Titre: Title:	High strain rate micro-compression for crystal plasticity constitutive law parameters identification
Auteurs: Authors:	Simon Breumier, Sergio Sao-Joao, Aillani Villani, Martin Lévesque, & Guillaume Kermouche
Date:	2020
Type:	Article de revue / Article
Référence: Citation:	Breumier, S., Sao-Joao, S., Villani, A., Lévesque, M., & Kermouche, G. (2020). High strain rate micro-compression for crystal plasticity constitutive law parameters identification. Materials and Design, 193, 17 pages. https://doi.org/10.1016/j.matdes.2020.108789

URL de PolyPublie: PolyPublie URL:	https://publications.polymtl.ca/45156/
Version:	Version officielle de l'éditeur / Published version Révisé par les pairs / Refereed
Conditions d'utilisation: Terms of Use:	Creative Commons Attribution 4.0 International (CC BY)

Titre de la revue: Journal Title:	Materials and Design (vol. 193)
Maison d'édition: Publisher:	Elsevier Ltd
URL officiel: Official URL:	https://doi.org/10.1016/j.matdes.2020.108789
Mention légale: Legal notice:	©2020 The Authors. Published by Elsevier Ltd. This is an open access article under the CC BY license (http://creativecommons.org/licenses/by/4.0/).

Materials and Design 193 (2020) 108789

Contents lists available at ScienceDirect

Materials and Design

journal homepage: www.elsevier.com/locate/matdes

High strain rate micro-compression for crystal plasticity constitutive law parameters identification

S. Breumier [a,*], S. Sao-Joao [a], A. Villani [a], M. Lévesque [b], G. Kermouche [a]

[a] *Mines Saint-Etienne, Univ Lyon, CNRS, UMR 5307 LGF, Centre SMS, F - 42023 Saint-Etienne, France*
[b] *Département de Génie Mécanique, École Polytechnique de Montréal, C.P. 6079, Succ. Centre-ville, Montréal, Québec H3C 3A7, Canada*

HIGHLIGHTS

- CPFE viscoplastic coefficients were uniquely identified using microcompression tests up to 100/s in the [100] orientation
- The problem well-conditioning result from strain rate localization in the shear bands
- Microcompression tests revealed an orientation dependent strain-rate sensitivity

GRAPHICAL ABSTRACT

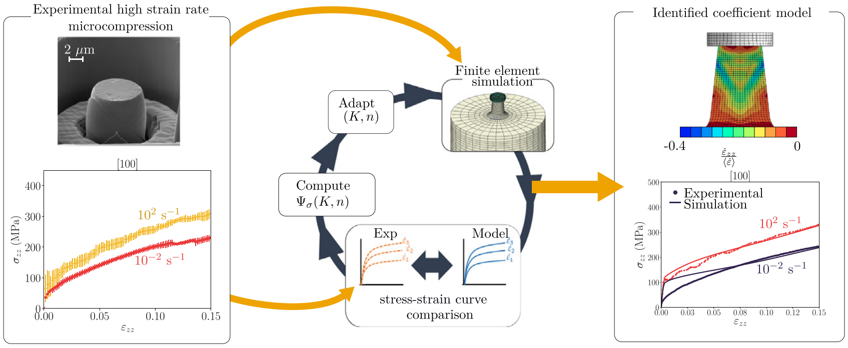

ARTICLE INFO

Article history:
Received 19 February 2020
Received in revised form 6 April 2020
Accepted 5 May 2020
Available online 19 May 2020

Keywords:
Micropillar compression
Crystal plasticity finite element
Inverse identification
Identifiability analysis

ABSTRACT

Microcompression tests were performed on single crystal copper micropillars at 10^{-2} s^{-1} and 10^2 s^{-1} in the [100], [110] and [111] orientations, to provide inputs for crystal plasticity strain rate sensitive parameters inverse identification. The identification procedure used full pillar geometry finite element simulations. An identifiability indicator based on the cost function's hessian matrix approximate close to the minimum was used to assess the uniqueness and stability of the identified coefficients. Experimental microcompression tests displayed a strain rate sensitive behaviour in the [100] crystal orientation. The [110] and [111] orientations were less sensitive and were not used for identification. Stress-strain curve sensitivity plots revealed that the higher the strain rate, the better the sensitivity. This was attributed to high strain rates concentration in the shear bands as the strain rate increases. Identification on experimental data well represented the single crystal strain rate sensitivity in the [100] orientations. A unique solution was found using only a single orientation.

1. Introduction

Shot-peening is a mechanical surface treatment that consists in projecting high velocity particles onto a ductile material surface. It is widely used to enhance material's fatigue life by subsurface hardening [38] and compressive residual stresses introduction [7].

Modeling such process requires the knowledge of the treated material's behaviour for strain rates ranging up to 10^6 s^{-1} [23]. Thus, parameters identification for such models is classically performed based on Split Hopkinson Pressure Bar tests (SHPB) [12,15,35,41]. However,

---

* Corresponding author.
E-mail address: simon.breumier@emse.fr (S. Breumier).

https://doi.org/10.1016/j.matdes.2020.108789

SHPB remains a macroscopic mechanical test since the solicited volumes range from a few cubic millimeters to a few cubic centimeters [1]. Thus it cannot be used to characterize material's surface behaviour as it is only applicable on low surface to volume ratio specimens. Dynamic indentation was also used by several authors [22,37] to obtain metals high-strain rates load displacement curves for plastic zone radius down to a few hundreds of micrometers [1].

However, recent studies [2,4,26,34] pointed out the necessity to model the shot-peening process at the grain scale. Musinski et al. [26] modeled the stress and strain redistribution in a shot-peened polycrystal with a Crystal Plasticity Finite Element framework (CPFE). Several fatigue cycles were then simulated on the resulting field. It revealed that an heterogeneous strain distribution influences the global stress relaxation through the fatigue cycles, which supported previous experimental studies [7].

Breumier et al. [2] analyzed the residual stress field induced by spherical indentation on copper single crystals with various orientations using High Resolution Electron BackScattered Diffraction (HR-EBSD) and CPFE analyses. It revealed that a spherical loading could induce tensile stresses at the grain scale for several orientations.

Castro-Moreno et al. [4] modeled several impacts on polycrystalline Representative Elementary Volumes (REV) with various grain sizes. The initial grain size only had an impact on the residual stress distribution at the grain level. Accurate local crystal plasticity models are therefore required to model the process at this scale.

The previous studies relied on crystal plasticity finite element frameworks (CPFE) whose input properties were extracted from macroscopic SHPB or cyclic tests. High strain rate tests performed at the crystal scale are however required to identify CPFE coefficients representative of the material behaviour during peening. Macroscopic tests such as SHPB are therefore highly impractical in such context as it is usually difficult to produce large single crystals for most alloys shot peened in the industry [42]. Also, tests used for identification must be representative of the surface behaviour as the depth affected by shot-peening is usually of a few hundreds of microns.

Nanomechanical tests such as micropillar compression could provide such local measurements. The test consists in compressing a micron-sized pillar using an instrumented diamond flat-punch to generate a load displacement curve. It therefore provides local stress-strain curves at the grain scale. Cruzado et al. [5] used such test for material parameters identification at low strain rates. The authors performed microcompression tests on a nickel-based super alloy in single slip and double slip conditions. The constitutive framework coefficients were deduced directly from the load displacement curves in single slip orientations. However, the study did not investigate the well-posedness of the inverse problem. Also, the proposed methodology could not be used on materials for which single crystals cannot be produced as it requires microcompression in perfect single glide conditions. When multiple gliding planes are activated, the load displacement curves can hardly be interpreted analytically as the pillar strains are highly heterogeneous.

Several works used Finite Element Model Updating (FEMU) to obtain crystal plasticity coefficients using experimentally obtained heterogeneous fields [10,31,36]. The method consists in varying the input material parameters of a finite element model to minimize the difference between experimental and predicted observation fields. It is therefore a promising methodology for crystal plasticity coefficients identification on multiple glide pillar compression tests as it would consider the heterogeneous straining of the pillar during identification. To the author's knowledge, FEMU parameter identification using micropillar compression load-displacement curves has never been performed.

Using a piezo-based sensor with high eigen-frequencies, Guillonneau et al. [11] recently performed microcompression tests at strain rates up to 10^3 s^{-1} on nanocrystalline Nickel specimens. Such test procedure provides useful data for parameters identification at high strain rates, at the local scale. Also, microcompression at high strain rates has never been performed on single crystals.

This work investigates the possibility to obtain a unique solution of a CPFE framework strain rate dependent coefficients by FEMU using high strain rates micropillar compression on single crystal copper. This work aims to develop a methodology for identification of a single crystal high strain rate surface behaviour. The well-posedness of the inverse problem was thoroughly investigated using an identifiability indicator. This ensures that the chosen experimental conditions contains sufficient information for identification, which has not yet been investigated using micropillar compression tests. Copper single crystal has been extensively studied since the early days of crystal plasticity and was thus chosen to validate the proposed methodology.

The paper is organized as follows: Section 2 presents the experimental as well as the numerical models and identification methodology used in the study. Section 3 details the performance obtained using the inverse identification methodology, first, on a virtual material, then, on the experimental results. Finally Section 4 discusses and concludes this paper.

2. Materials and methods

2.1. Materials and specimen preparation

Micropillar compression tests were conducted on pure single crystal copper specimens obtained by directional solidification using a conventional Bridgman apparatus. Three crystals were grown in the [111], [110] and [100] orientations, respectively. A 1×1 cm square with a thickness of 0.5 cm was cut from each specimen using a diamond wire saw.

The samples were mechanically polished using SiC grit paper from P400 to P1000 and then electro-polished to provide a sufficiently good surface finish for EBSD observations. This was necessary to obtain the single crystal's exact orientation (given in Table 1) by conventional Hough indexation, using an HKL system (Oxford instrument) composed of a NordlysII camera and the Channel 5 software suite.

Micropillars were machined by Focus Ion Beam (FIB) machining using a Thermo Scientific Helios NanoLab DualBeam microscope. First, high currents (30 kV, 2.5 A) were used to dig the raw pillar shape. Smaller currents (30 kV, 80 pA) were then used to refine the geometry. Size effects were investigated using 3 μm, 6 μm and 8 μm diameters pillars for every orientation. Compression tests at different velocities were performed on 6 μm and 8 μm diameters pillars. The targeted pillar diameter to height ratio was 1:2, as suggested by Zhang et al. [40] to prevent pillar buckling.

The exact pillar dimensions were required to reproduce the pillar geometry in the numerical simulations. Fig. 1 shows the measured pillars dimensions (top (D_t) and bottom (D_d) diameters and height (h)). The pillars dimensions means and standard deviation are

Table 1
Single crystal's experimentally measured orientation Euler angles.

Target	$\phi_1(^\circ)$	$\Phi(^\circ)$	$\phi_2(^\circ)$
[100]	128,2	3,42	59
[110]	84,15	44,22	0.1
[111]	290,96	51,37	47,22

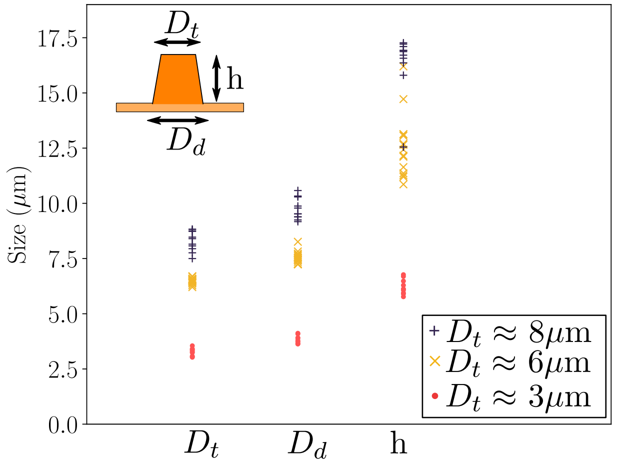

Fig. 1. Pillars top and bottom diameters (D_t and D_d) and height (h) for the three crystal orientations. Targeted pillar top diameters were 3 μm, 6 μm and 8 μm. The target diameter to height ratio was 1:2.

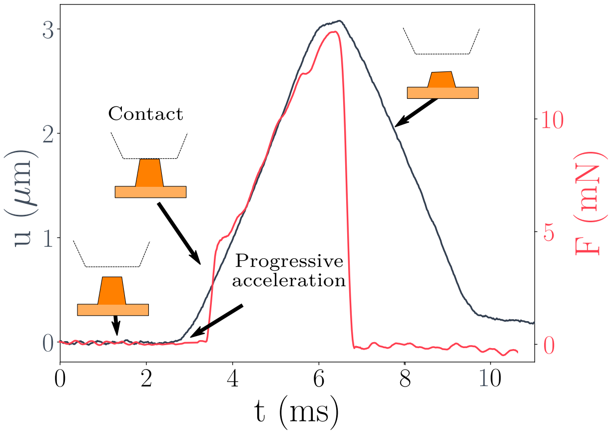

Fig. 2. Example of a typical high dynamic imposed displacement profile u(t) and resulting measured load F(t). The indenter accelerates progressively to reach the pillar surface at a constant displacement rate. The sudden load increase provides the time of contact. This prevents from triggering the actuator natural frequencies.

summarized in Table 2. The measurements were performed directly on Scanning Electron Microscope (SEM) pictures, using one observation angle.

2.2. High dynamic micropillar compression tests

Micropillar compression tests were conducted using an ALEMNIS in-situ nanoindenter apparatus in a Zeiss Gemini supra 55VP Scanning Electron Microscope (SEM). The test consists in compressing a small pillar with an instrumented diamond flat-punch to extract the local load-displacement curve. The load applied on the specimen was measured with a 50 kHz acquisition rate using a high dynamic SmarTip load cell placed under the specimen holder. Such an apparatus can reach high strain rate microcompression testing up to 10^3 s^{-1}, as detailed in the work of Guillonneau et al. [11].

Pillars were compressed with nominal strain rates of 10^{-2} s^{-1} and 10^2 s^{-1}. Note that the nominal strain rate is defined as the maximum displacement divided by the pillar initial height and by the compression time.

Fig. 2 shows a typical displacement profile imposed to the indenter during a microcompression test. For high strain rate tests, the pillar is not in contact with the indenter at its initial position. The indenter accelerates progressively to reach the targeted constant displacement rate without triggering the piezoStack actuator natural frequencies. For each test, the contact onset was taken as the time for which the measured load exceeds the average noise value. The critical acceleration to reach before the actuator vibrates was estimated through several tests in the void.

The inertial force induced by the indenter acceleration was also investigated and corrected using sinus displacement profiles in the SEM void, following the methodology detailed by Guillonneau et al. [11].

Table 2
Micropillar dimensions means and confidence interval (95%) for the three aimed sizes.

Target D_t	D_t	D_d	h
3 μm	3.27 ± 0.1	3.81 ± 0.11	6.21 ± 0.20
6 μm	6.48 ± 0.07	7.54 ± 0.13	12.57 ± 0.69
8 μm	8.31 ± 0.26	9.74 ± 0.27	16.39 ± 0.76

The measured displacement u_{mes} was corrected to remove the influence of the frame elastic deformation using:

$$u_{pil} = u_{mes} - \frac{F}{K_{frame}}, \tag{1}$$

where u_{pil}, F, K_{frame} correspond to the pillar displacements, the measured load and the frame stiffness respectively. Copper being a very ductile material, the influence of the substrate displacement was considered negligible. The load displacement curve was filtered to remove part of the experimental noise using a built-in moving average smoothing filter (10 points length).

All the microcompression data generated for this article is available for download as detailed in the Data availability section. Each pillar is associated to a file containing the raw and the treated load displacement curve, as well as SEM pictures of the pillar both before and after compression.

2.3. Crystal plasticity constitutive behaviour

The single crystal constitutive behaviour was modeled using the Meric-Cailletaud large-strain formulation crystal plasticity framework [2,25]. The deformation gradient **F** was decomposed between its elastic and plastic contributions, respectively $\mathbf{F}^e$ and $\mathbf{F}^p$, as:

$$\mathbf{F} = \mathbf{F}^e \cdot \mathbf{F}^p, \tag{2}$$

where · denotes the dot product. The plastic part was related to the slips occurring in the different slip systems through

$$\mathbf{F}^p \cdot \left(\mathbf{F}^p\right)^{-1} = \sum_{s=1}^{N} \gamma^s \mathbf{m}^s \otimes \mathbf{n}^s, \tag{3}$$

where γ^s is the s-th slip system shear strain rate, N is the number of activable slip systems (12 for face-centered cubic structures) and $\mathbf{m}^s$ and $\mathbf{n}^s$ are unit vectors representing respectively the slip direction and the normal to the slip plane.

The stress τ^s projected on each slip system was related to the system's shear strain rate according to a Norton law where

$$\gamma^s = \left\langle \frac{f^s(\tau^s)}{K} \right\rangle^n, \tag{4}$$

with <. > being the Macaulay brackets, defined as:

$$<x> = \begin{cases} 0 & \text{if} \quad x<0 \\ x & \text{if} \quad x\geq 0 \end{cases},$$

K and n being material constants, which accounts for the material's strain rate sensitivity. An isotropic hardening term r^s was added to the flow rule f^s as

$$f^s = |\tau^s| - r^s. \tag{5}$$

The hardening term r^s results from the interactions between the different dislocation slip systems modeled by

$$r^s = R_0 + \sum_{q=1}^{N} h_{sq}(R_q - R_0), \tag{6}$$

with

$$R_q = R_0 + Q\left(1 - e^{-v^q b}\right), \tag{7}$$

where R_0 is the critical resolved shear stress, Q and b are two phenomenological constants, v^q is the cumulated plastic slip for the q-th system and h_{sq} is the interaction coefficient between systems (s) and (q). For Face-Centered Cubic (FCC) structures, the interaction matrix contains six different coefficients that account for the interaction phenomena listed in Table 3.

Table 3
Hardening interaction matrix parameters [25].

h_1	h_2	h_3	h_4	h_5	h_6
Self-hardening	Coplanar	Hirth lock	Collinear	Glissile	Lomer junction
1	4.4	4.75	4.75	4.75	5

2.4. Material parameters identification

2.4.1. Finite element model updating (FEMU) procedure

The Norton law K and n coefficients were identified using FEMU to assess the material's strain rate sensitivity. The finite element model developed for identification used the experimentally measured pillars geometries and is detailed in Section 2.5. The procedure was first tested using load-displacement curves generated by a virtual material. Those curves were obtained using the full pillar geometry simulations with coefficients $K = 7$ MPa $s^{1/n}$ and $n = 4$.

The identification procedure consisted in varying the Norton law coefficients K and n to minimize the following cost function:

$$\Psi_\sigma(K,n) = \frac{1}{2T}\sum_{m=0}^{N_{exp}}\sum_{t=0}^{T}\left(\frac{\sigma_m(\varepsilon(t),K,n) - \sigma_{m,\,exp}(\varepsilon(t))}{\max\limits_t(\sigma_{m,\,exp}(\varepsilon(t)))}\right)^2. \tag{8}$$

In Eq. (8), T is the number of acquisition points which was chosen as 100 for every simulation, N_{exp} is the number of stress-strain curves used for identification, $\sigma_{m,\,exp}(\varepsilon(t))$ and $\sigma_m(\varepsilon(t),K,n)$ are respectively the experimental and predicted stress. Despite the finite strain formulation of the crystal plasticity framework presented in Section 2.3, the identification procedure was restricted to the small strain range of the curves. The experimentally measured stress was therefore computed using

$$\sigma_{m,\,exp}(t) = \frac{P_{m,\,exp}(t)}{\pi r_{avg}^2}, \tag{9}$$

where $P_{m,\,exp}(t)$ is the experimental load at time t and r_{avg} is the average of the pillar initial top and bottom radii.

Table 4
Elastic coefficients [25].

C_{11} (MPa)	C_{22} (MPa)	C_{44} (MPa)
159,300	122,000	81,000

Note that using the stress defined as in Eq. (9) for identification is equivalent to using the load as the identification variable. In the present work, the stress was used to compare the identification performance of the present model with a single-element model, as presented in Appendix E.

The Levenberg-Marquardt algorithm was used to minimize Ψ_σ. The coefficients used as a first guess in the procedure were those identified by Meric et al. [25] and recalled in Tables 3, 4 and 5.

To compare the experimentally measured and predicted data at the same strain values, the experimental stress was interpolated linearly at the strain values chosen for comparison. Only the loading part of the curve was used.

2.4.2. Identifiability indicator

Given the computational cost of the full pillar geometry model, the identifiability indicator I defined in the work of Richard et al. [27,30–32] was used as an indicator of the solution uniqueness and stability. This indicator is based on the cost function hessian close to the cost function minimum. It is defined as:

$$I = \log_{10}\left(\frac{\lambda_{max}}{\lambda_{min}}\right), \tag{10}$$

where λ_{max} and λ_{min} are the eigenvalues extrema of the approximated dimensionless hessian matrix close to the solution, defined as:

$$\overline{H}_{ij} = \sum_{t=0}^{T}\sum_{m=1}^{N_{exp}}\frac{\partial\overline{P_m}(t)}{\partial\theta_i}\frac{\partial\overline{P_m}(t)}{\partial\theta_j}. \tag{11}$$

In the above, $\frac{\partial\overline{P_m}(t)}{\partial\overline{\theta_i}}$ is the load-displacement curve sensitivity to the θ_i parameters. This sensitivity was here defined as:

$$\frac{\partial\overline{P_m}(t)}{\partial\overline{\theta_i}} = \frac{P_m(t,\theta_i+\delta\theta_i) - P_m(t,\theta_i)}{\max\limits_t(P_m(t,\theta_i))\delta\sqrt{T}}, \tag{12}$$

where δ is a perturbation factor chosen as 5%. Eq. (12) defines the dimensionless load variation to a perturbation δ on parameter θ_i. Normalization by $\sqrt{T}$ provides a sensitivity definition consistent with Eq. (8) and ensures that I does not depend on the number of acquisition points. A good identifiability of the solution can be achieved for $I \leq 2$, as explained by Richard et al. [32].

As pointed out by Renner et al. [30], normalization by $\max\limits_t(P_m(t,\theta_i))$ is equivalent to consider an absolute uncertainty on the load measurement. Such assumption relies on the highly repeatable

Table 5
Norton law and isotropic hardening parameters [3].

K (MPa $s^{1/n}$)	n	R_0 (MPa)	Q (MPa)	b
5	10	10	6	15

experimentally measured stress for a given strain at a given strain-rate, as well as by the high signal to noise ratio provided by the piezo load sensor.

2.5. Finite element model

The experimentally measured pillar geometry was used to model the microcompression experiment. The model used the Abaqus 2018 software coupled with Zset using the Zmat module. The pillar geometry and mesh is represented in Fig. 3. Substrate dimensions were chosen to prevent any effects of the boundary conditions on the load displacement curve (see Appendix A). The mesh was composed of linear reduced hexahedric elements (C3D8R) to prevent locking effects arising from high plastic incompressibilty [9].

Hourglass was corrected by adding an artificial stiffness to the elements. Only a small correction was necessary (15 MPa) as little hourglass was observed. The mesh size varied from 0.14 μm in the pillar to 1.4 μm in the substrate and was determined after a convergence study (see Appendix B).

Using the converged model, the computational time for each simulation was between six to ten hours using 4 threads on an Intel Xeon Gold 6132, 2.6 GHz CPU with Abaqus 6.14 version.

The indenter was explicitly modeled as a rigid surface to account for the friction occurring between the tip and the top pillar surface. The friction coefficient f was set to 0.2 to prevent pillar buckling (as it was not observed experimentally). The influence of a friction coefficient variation on the load displacement curve was negligible for $f \geq 0.2$, as presented in Appendix C. The indenter experimental displacement profile was imposed to the rigid indenter reference point.

Internal heat generation induced by the pillar high strain rate plastic straining was not considered in the model as it was considered negligible on the pillars material properties, as detailed in Appendix F.

3. Results

3.1. Virtual material identifications

Inverse identification was first performed on virtual data generated using the full pillar geometry model with $K = 7$ and $n = 4$. The solution obtained is given in Table 6. The Levenberg-Marquardt minimization found the virtual material coefficients in 25 iterations with a relative error of 0.57% and 4.75% for K and n, respectively. The resulting identifiability indicator value was $I = 1.5$. This confirms that the overall identification procedure could provide a satisfying solution in terms of uniqueness and stability.

Table 6
Solution of the identification procedure using the real pillar geometry compared with the chosen virtual material parameters. The discrepency between the input and identified K and n are respectively of 0.57% and 4.75%.

	K (MPa s$^{1/n}$)	n
Virtual material	7	4
Identification solution	6.96	3.81

Fig. 4 (a) shows the L_2 norm of the sum of all load sensitivities to a 5% variation of the K and n coefficients around the cost function minimum, computed as:

$$\left\| \frac{\partial \overline{P_m}(t)}{\partial \overline{\theta_i}} \right\|_2 = \sqrt{\sum_{k=0}^{T} \frac{\partial \overline{P_m}(t)}{\partial \overline{\theta_i}}^2}. \tag{13}$$

Fig. 4 (a) reveals that the variation of both coefficients have a similar effect on the global predicted load-displacement curves absolute amplitudes.

Fig. 4 (b), (c), (d) shows the variation of the load sensitivity with the applied displacement for each computed nominal strain rates. The influence of the two coefficients on the curve is non collinear for each strain rate. Also, the sensitivity values for a given displacement reveals that the higher the nominal strain rate, the higher the sensitivity. Experimental load-displacement curves at the highest strain rates hence provides more valuable data for identification as it is more sensitive to the coefficients variation.

3.2. Identification on microcompression tests

3.2.1. Experimental results

Size effects were investigated using the three pillar sizes as presented in Appendix D. The 3 μm sized pillars systematically presented a pronounced size effect and higher result variability and were therefore not accounted for. The 6 μm-sized pillars were used for high strain rate compression (since the smaller pillars allows to reach the highest strain

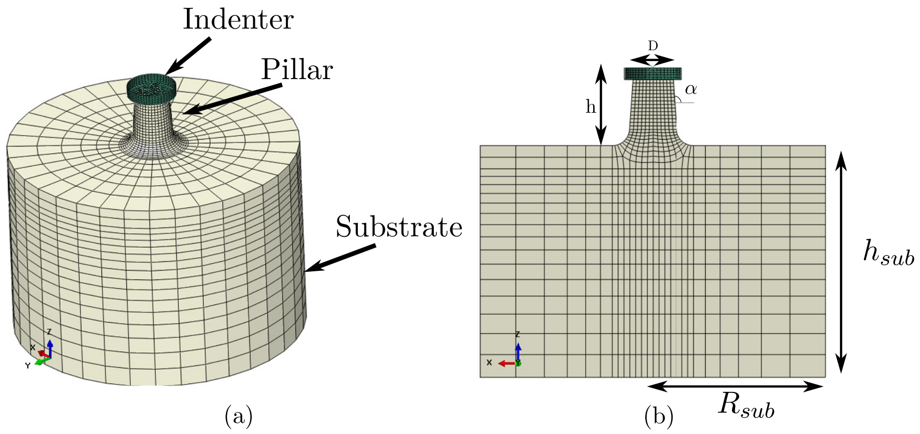

Fig. 3. (a) Finite element mesh used for the micropillar compression simulation. The indenter was modeled as rigid. The mesh was refined in the pillar and is progressively coarsened toward the substrate borders. (b) Geometry of the finite element model. h_{sub} and R_{sub} are the substrate height and radius. h, D and α are the pillar height, diameter and tapper angle.

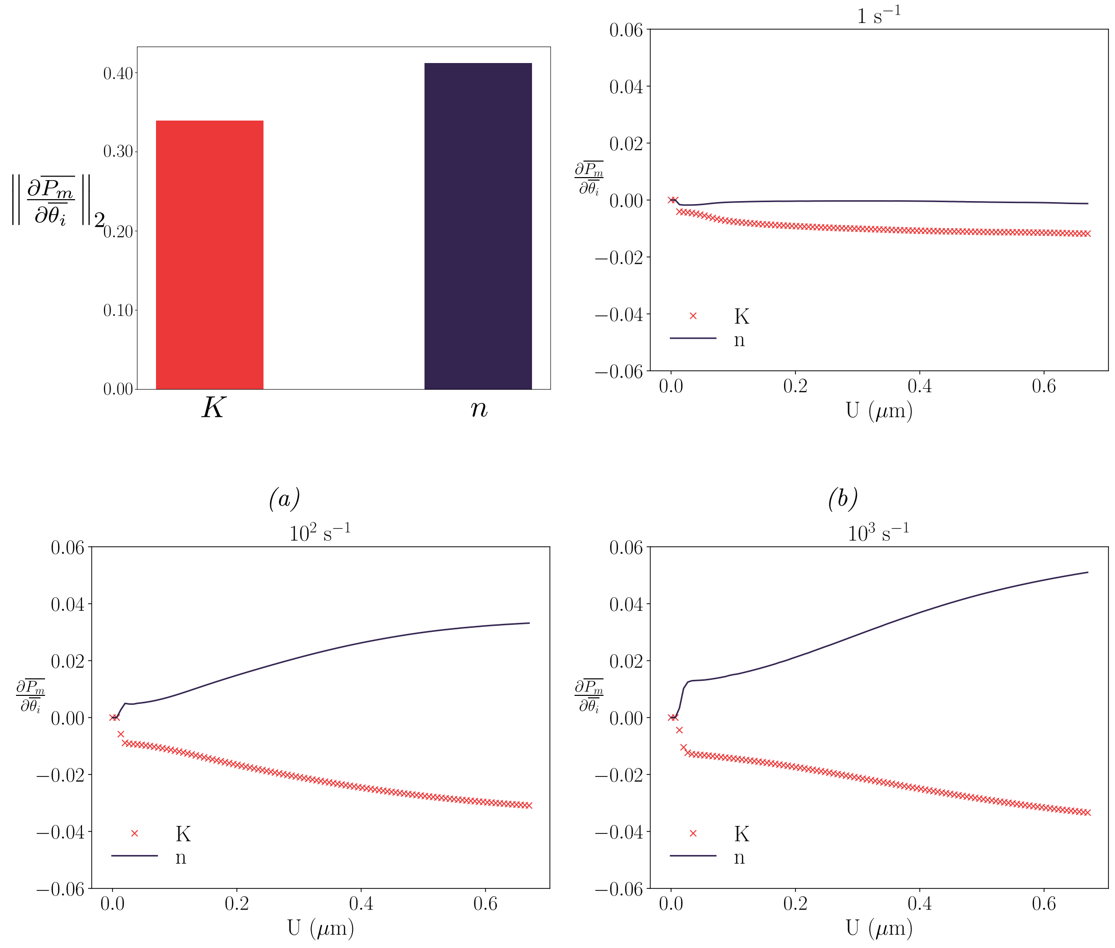

(a) (b)

(c) (d)

Fig. 4. Load displacement curve sensitivity to a 5% varation of K and n close to the cost function minimum using the experimentally measured pillar geometry. (a)L_2 norm of the total sensitivity. Evolution of the predicted load sensitivity with the imposed displacement at (b)1 s^{-1}, (c)10^2 s^{-1} and (d)10^3 s^{-1} nominal strain rates. The load displacement curve is sensitive to a variation of both coefficients with a similar amplitude. Sensitivities for each strain rates reveals that the higher the nominal strain rate, the higher the load sensitivity amplitude.

rates). The 8 μm pillars were used for low strain rate compression (as they presented less variability at low strain rates than the 6 μm pillars).

Fig. 5 shows the stress-strain curves obtained by microcompression testing at different strain-rates for the three different orientations. In the [100] orientations, pillars #3 and #4 presented a slightly different behaviour from the others. Fig. 7 shows the three 6 μm diameter pillars deformed shapes after microcompression at $<\varepsilon> \approx 10^2$ s^{-1}. Pillars #1 and #2 both presented a clearly marked double-slip pattern. Pillar #3 presented a barrel shape with no sign of slip bands. Pillar #3 will therefore not be considered for material parameters identification as it encountered different plasticity mechanisms than the other pillars, which could not be represented using the presently used crystal plasticity framework.

Pillar #4 stress-strain curve presented a constant stress shift when compared with other stress-strain curves at $<\varepsilon> \approx 10^{-2}$ s^{-1}. As this compression test was performed first, load drifts due to SEM void stabilization sill occurred. Such drift might explain the stress shift observed for pillar #4. This curve was therefore also not considered for material parameters identification.

Fig. 6 shows the averaged microcompression curves obtained after putting aside pillars #3 and #4. A significant strain rate effect was observed for microcompression in the [100] orientation. Also, the stress-strain behaviour presented a good repeatability for a given approximated strain rate. A weaker effect was observed in the [110] and [111] orientations. The large results variability for a given strain rate prevented quantitative assessment of the stress-strain curve sensitivity in these orientations.

The overall good repeatability of the stress-strain curves suggest that the strain-rate dependency observed does not depend on the pillar size, owing to the statistical nature of size-effects. Several tests would be required to confirm such results, which is not in the scope of this paper. The pillar diameters used were however consistent with the literature [6,20]. Kiener et al. [18] estimated that no size effect would occur in copper micropillars with diameters larger than 5 μm.

In the following, the stress-strain curves obtained in the [100] orientations were used for strain-rate sensitivity material parameters identification as it presented the most repeatable results. The assessment of the solution uniqueness was performed to ensure that a single orientation was sufficient for identification.

3.2.2. Material parameters identification

The identification procedure using the real pillar geometry was applied to the experimental load-displacement curves obtained with the

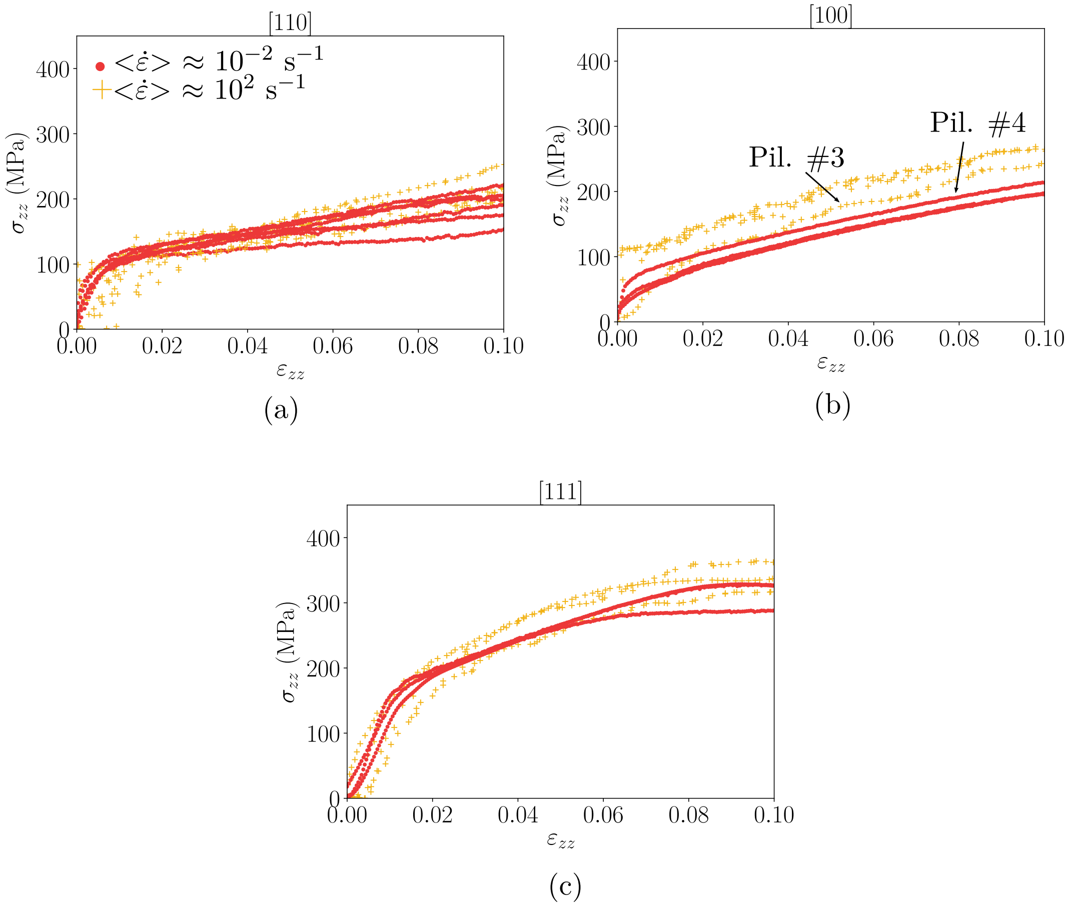

(a)

(b)

(c)

Fig. 5. Microcompression stress-strain curves for (a) [110], (b) [100] and (c) [111]-oriented pillars 6 and 8 μm top diameters compressed at average strain-rates of 10^{-2} s^{-1} and 10^{2} s^{-1}. Stress-strain curves measured in the [110] orientation presented a larger discrepancy then the others. Pillar #3 and #4 were discarded for the [100] orientation.

[100] crystal orientation at two different strain rates. The resulting stress-strain curves obtained with the identified parameters are presented in Fig. 8 (a).

The solution represented well the copper specimen hardening strain-rate sensitivity in the [100] orientations. The experimentally observed and numerical yield stress evolution with the strain rate were however different.

The stress-strain curve obtained using this solution in the [111] crystal orientation were compared with the experimental results in Fig. 8 (b). The strain-rate sensitivity orientation-dependency was not well reproduced by the model.

The identifiability indicator computed after identification was $I = 1.31$. Fig. 9 shows the cost function computed for a hundred different parameters and confirms the well-posedness of the inverse problem. This confirmed the quality of the solution found in terms of uniqueness and stability. Also, it reveals that using a single orientation for identification is sufficient to obtain a unique solution. Using both orientation for identification would therefore not have resulted in an orientation dependent sensitivity closer to the experimental one.

The material's behaviour at low strain rate was also very similar to the experiment. This gives confidence in the physical relevance of the hardening and interaction coefficients taken from the literature.

4. Discussion

4.1. Strain rate induced stress heterogeneities

Fig. 10 represents the σ_{zz} distribution in the pillars, for the virtual material simulations and for three different strain rates. The figure reveals that the higher the strain rate, the more heterogeneous the stress state is in the pillar. As the strain rate increases, the stress distribution changes from a uni-modal to a bi-modal shape. For high strain rates, the pillar can therefore no longer be considered as homogeneously loaded.

Fig. 11 shows the $\sigma_{zz} - <\sigma_{zz}>$ variations at the pillar center in the *x*-*z* plane. The mean stress values has been subtracted from the stress to compare the changes in stress distribution with the strain rate, independently of the stress amplitude variations. At 1 s^{-1}, the highest stresses are concentrated in the shear bands. The stress state in the zone below and above those bands is similar. This zone therefore represents the unique peak observed in the stress distribution. At 10^{2} s^{-1} and 10^{3} s^{-1}, the stress amplitude raises above the shear bands but not bellow. This results in a bimodal stress-distribution.

To better understand these heterogeneities, the strain-rate variations at the pillar center in the *x*-*z* plane, normalized by the pillar average strain rate, were represented in Fig. 12, for the three velocities. The figure shows a highly heterogeneous strain rate distribution in the pillar. The highest strain rates were found in the slip bands. Fig. 13 shows the strain rate distribution in the whole pillar volume. The figure confirms that a bimodal strain rate distribution is also found in the whole pillar volume for all the modeled strain-rate.

This strain rate localization induces different strain mechanisms in the pillar since the global strain rate increases. Fig. 14 shows the equivalent von Mises plastic strain field at the pillar center. For low strain rates, plastic strains are localized in the slip bands, with higher values at the pillar surfaces. As the strain rate increases, the material in the shear bands

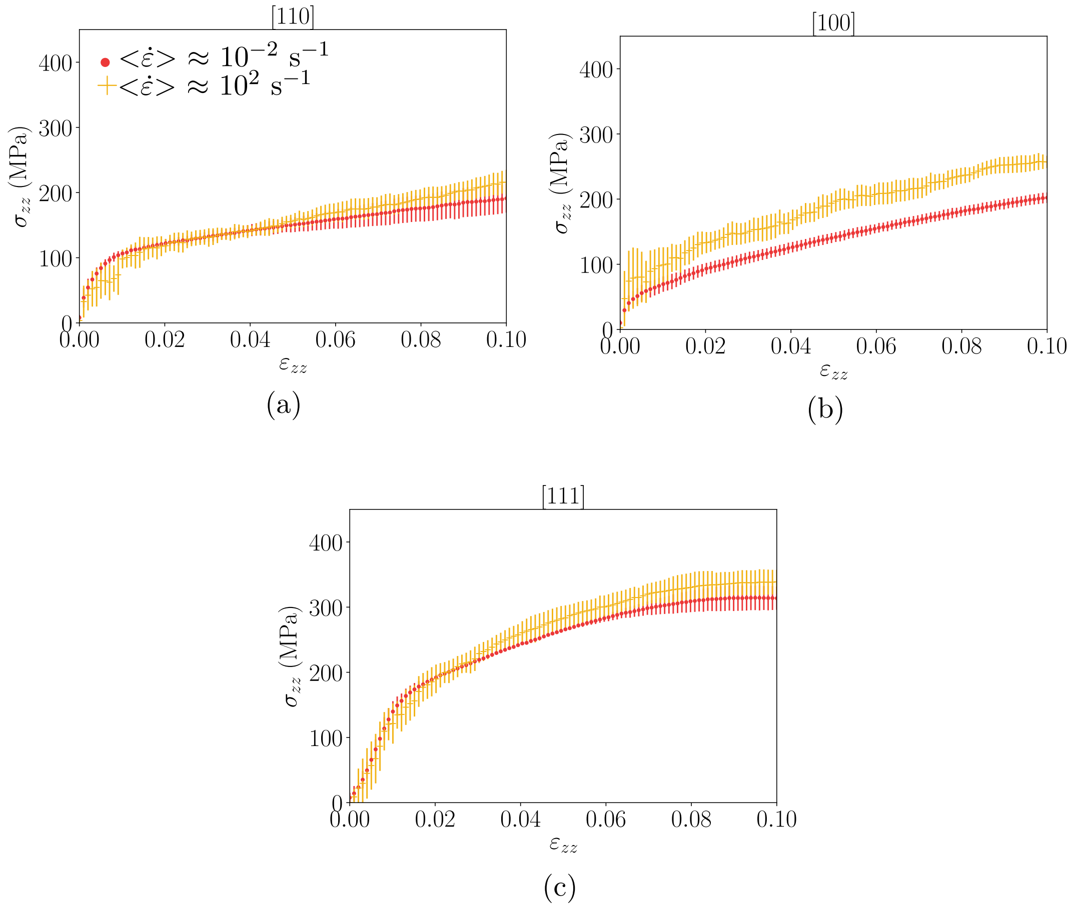

(a)

(b)

(c)

Fig. 6. Microcompression stress-strain curves mean and standard deviation for (a) [110], (b) [100] and (c) [111]-oriented pillars compressed at average strain-rates of 10^{-2} s^{-1} and 10^{2} s^{-1}. Hardening strain-rate sensitivity was observed for the [100] orientation. The stress-strain curves discrepancy in the [110] and [111] orientations prevents quantitative assessment of the orientation sensitivity.

requires higher stresses to strain further since it deforms more rapidly. This results in less plastic strains in the bands, when compared to those predicted for the low strain rate simulation. As yielding occurs in the bands, the material requires higher stresses to deform and the strain is therefore redistributed in the zone above the shear bands. This results in the plastic yielding of this zone, the bottom zone remaining elastic. This explains the bimodal stress state observed in Fig. 10.

There is therefore a structural effect, which enhances the apparent strain rate sensitivity influence on the load-displacement curve. As detailed in Appendix E, modeling the pillar as single element or using the experimental stress-strain curve for strain-rate sensitivity direct estimation cannot account for such structural effects. Such approximations therefore results in a non unique solution for the strain-rate coefficients.

This structural effect could explain that using only the [100] orientation was sufficient to obtain a good identifiability indicator value. The stress contrast induced in the pillar as the strain rate increases could explain the highest load sensitivity revealed in Fig. 4. However, the amplitude of this structural effect should

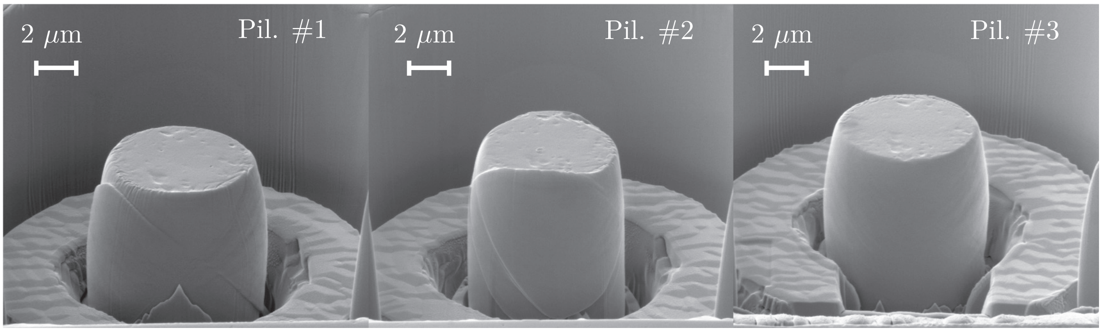

Fig. 7. 6 μm top diameter pillars deformed shapes after microcompression at $<\varepsilon> \approx 10^{2}\ \mathrm{s}^{-1}$. Pillars #1 and #2 both presented a clearly marked double-slip pattern. Pillar #3 presented a barrel shape with no sign of slip bands. The deformed pillar shapes explains the differences in the stress-strain curves observed in Fig. 5.

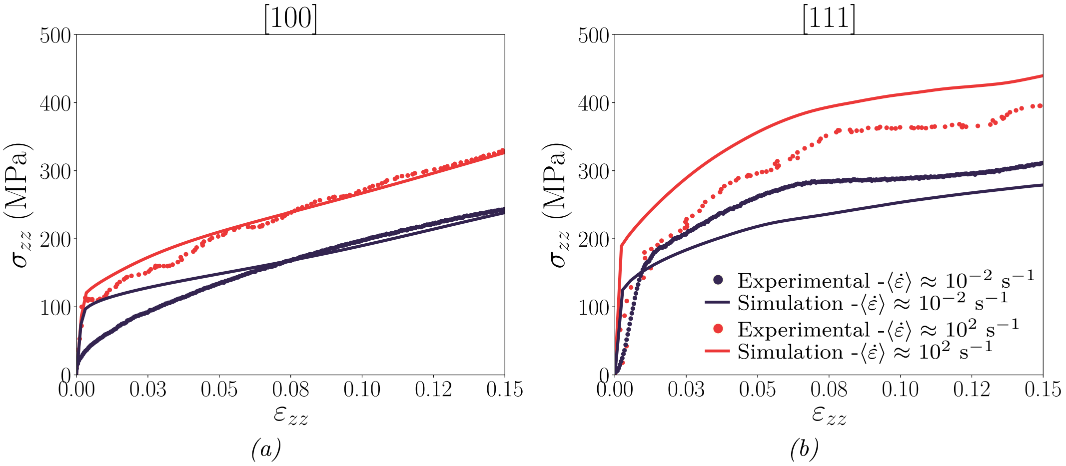

Fig. 8. Experimental and numerical stress-strain curves obtained after material parameters identification using the real pillar geometry, with the experimental data obtained in the [100] crystal orientation. (a) Comparison with the experimental curves used for identification. (b) Performance of the identified model in the [111] orientation. The model captured well the material's hardening strain-rate sensitivity in the [100] orientation. The yield stress dependency with the strain-rate was not well represented. Also, the strain-rate sensitivity orientation dependency was not well captured by the model either.

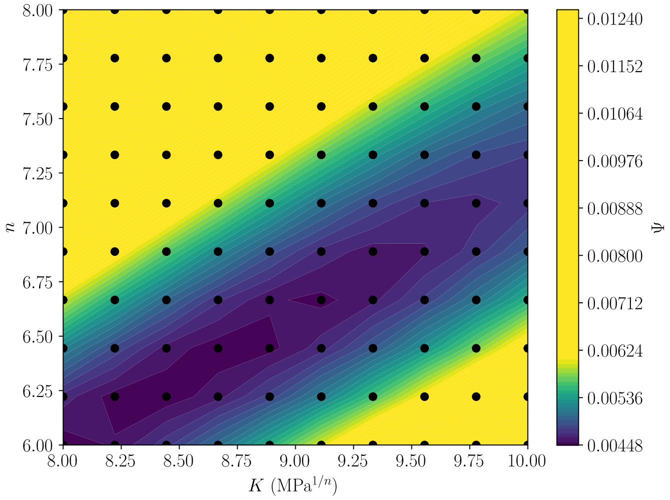

Fig. 9. Minimization problem cost function in the viscinity of the solution. The black dots represents the parameters used to plot the function. The convex shape of the function close to the equilibrium confirms the well-conditioned nature of the problem.

be related to the material's sensitivity. For low sensitivities, strain rate concentration in the slip bands would induce lower hardening contrasts as with the virtual parameter values used in this study.

4.2. Orientation-dependent strain-rate sensitivity

Copper strain rate sensitivity orientation dependency has already been observed in the literature [13,29]. Rawat et al. [29] performed SHPB (4.5 10^3 s^{-1}) and quasi-static (3.3 10^{-3} s^{-1}) tests on copper single crystals in the [100] and [110] orientations. Despite the different strain rate ranges, similar orientation dependent sensitivities were observed for the stress-strain curves. The [110] orientation presented almost no strain rate sensitivity, when compared to that observed for the [100] orientation. According to Horstemeyer et al. [13], this observation cannot simply be explained by the geometry of slip but more by the nature of dislocation interactions in a given slip system.

Wang et al. [39] performed dislocation dynamic simulation on fcc single crystals at different strain rates on three different orientations. The three different orientations presented differences in the cross-slip activity leading to higher dislocation dipole annihilation for the [111] and [211] oriented crystals as the strain rate increases. Such differences

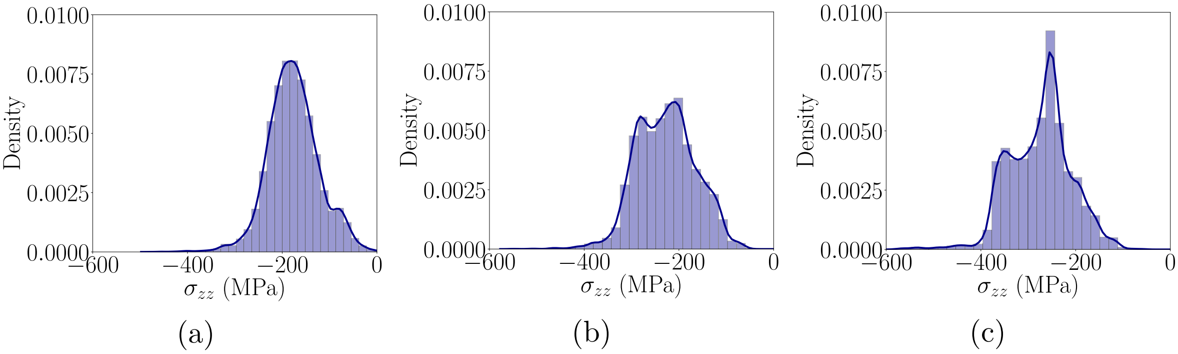

Fig. 10. Stress distribution in the pillar volumes obtained from the virtual material simulations using the real pillar geometry submitted to an average imposed strain rate of (a) 1 s^{-1}, (b) 10^2 s^{-1} and (c) 10^3 s^{-1}. A uniform stress distribution was found at 1 s^{-1}. Higher strain rates induced higher stress heterogeneities inside the pillar.

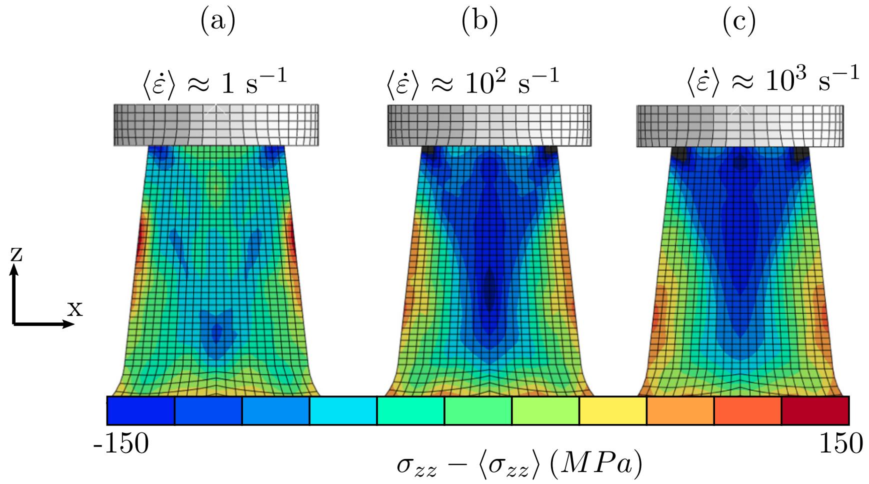

Fig. 11. σ_{zz} variations around the whole pillar σ_{zz} average, on the x-z plane, obtained from the virtual material simulations for an average imposed strain rate of (a) 1 s^{-1}, (b) 10^2 s^{-1} and (c) 10^3 s^{-1}. At 1 s^{-1}, the stress below and above the shear bands present similar values. At 10^2 s^{-1} and 10^3 s^{-1}, the stress above the pillar rises significantly, resulting in a bimodal stress distribution in the pillar volume.

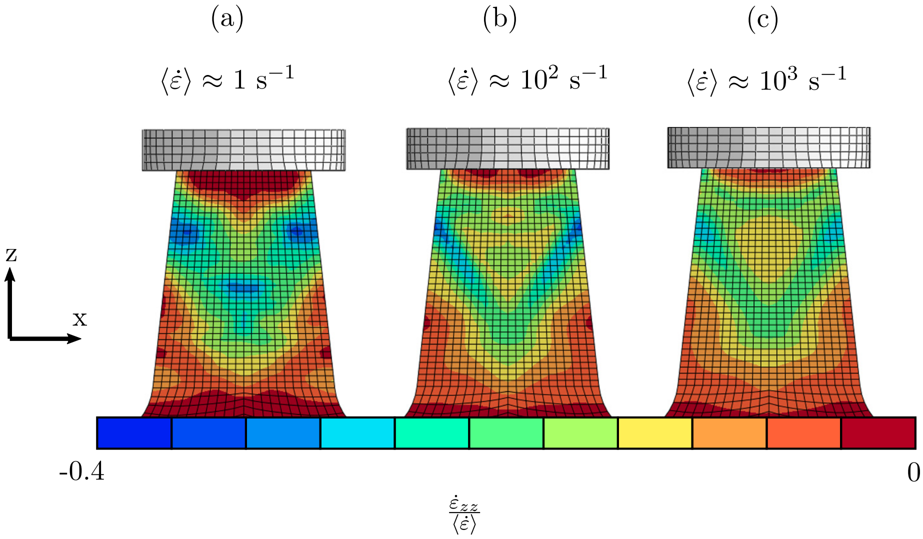

Fig. 12. Normalized strain-rate distributions in the pillar in the x-z plane obtained from the virtual material simulations for an average imposed strain rate of (a) 1 s^{-1}, (b) 10^2 s^{-1} and (c) 10^3 s^{-1}. For the highest velocity, the highest strain rates are concentrated in the shear bands.

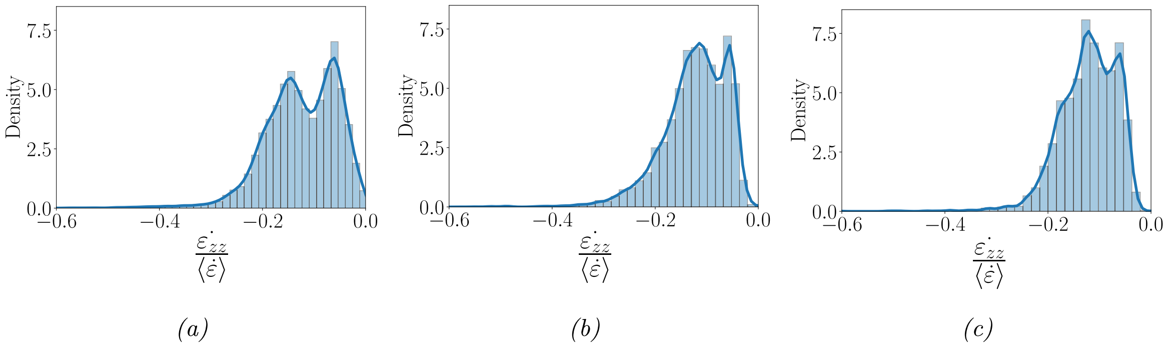

Fig. 13. Strain rate ε_{zz} distribution inside the pillar obtained from the virtual material simulations using the real pillar geometry at an average imposed strain rate of (a) 1 s^{-1}, (b) 10^2 s^{-1} and (c) 10^3 s^{-1}. A bimodal strain rate distribution is observed both at low and high strain rates in the pillar.

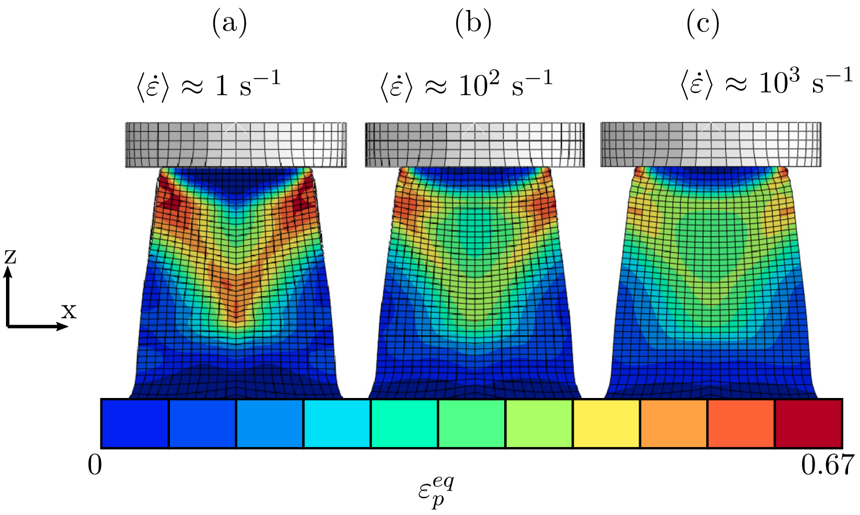

Fig. 14. Equivalent von Mises plastic strain ε_p^{eq} distribution in the pillar on the x-z plane obtained from the virtual material simulations at an average imposed strain rate of (a) 1 s^{-1}, (b) 10^2 s^{-1} and (c) 10^3 s^{-1}. At low strain rates, plastic strain is concentrated in the shear bands. As the strain rate increases, the top of the pillar plastifies more homogeneously, as higher stresses are required for further plastic straining in the shear bands.

in plasticity mechanisms could explain the anisotropic strain rate dependency observed in Fig. 6.

The mismatch in sensitivity orientation dependency between the model and experimental observations is therefore a consequence of the crystal plasticity model chosen. This was also observed by Khan et al. [17]. The authors used three different crystal plasticity frameworks to model single crystal compression at various strain rates (ranging from 10^{-4} s^{-1} to 10^3 s^{-1}). The first framework used a similar formulation as presented in Section 2.3 and could not account for orientation dependent strain rate sensitivity. The second model consisted in adding a strain rate dependant hardening behaviour, accounting for yield stress strain rate sensitivity. The predicted and experimentally measured stress strain curves were in good agreement but only for the orientation used for identification. The third approach used a dislocation based crystal plasticity model with a Kocks-Mecking evolution law. This approach captured well the single crystal strain rate sensitivity on the various orientation tested.

In such models, dislocations interactions and strain rate sensitivity are implicitly related by the dislocation evolution law. This could explain its good performances on several different orientations. This confirms that the Meric-Cailletaud framework is not relevant to model the crystal behaviour for a large strain rate range. However, dislocation based framework usually involves several parameters which could hardly be identified using experimental observations. An intermediate scale model would therefore be required for potential high strain rate industrial applications.

Also, such models could not account for the strain-rate dependent recovery mechanisms evidenced by Wang et al. [39] and could therefore fail to represent the highly anisotropic strain rate dependency observed in Fig. 6. Kocks et al. [19] and Galindo-Nava et al. [8] developed dislocation density based models accounting for a strain-rate dependent recovery. Finite element integration of such framework however requires further extensive work as it involve several numerical challenges. It was therefore left for future works.

This orientation dependent effect could however be used wisely for parameters identification. Indeed, micropillar compression enables to select the tested orientation and therefore the activated gliding systems - In contrast with nanoindentation testing for which all gliding systems are usually activated. It is therefore possible to select the most strain rate sensitive orientations to fully capture the material's viscoplastic behaviour.

Yield stress strain rate dependency is usually very subtle at intermediate strain rates for most face-centered cubic (fcc) materials [24]. The use of the Meric-Cailletaud framework for low strain-rates for those materials relies on the fact that strain-rate sensitivity only influences hardening. In this work, yield stress sensitivity was already visible at $<\varepsilon> \approx 10^2\ \mathrm{s}^{-1}$. Future works will focus on the validation of the proposed identification procedure using a more representative crystal plasticity framework.

In this work, copper was solely used to validate the proposed identification methodology. The results reveal that this methodology could provide a unique solution to crystal plasticity viscoplastic coefficients using a single crystal orientation, which, to the authors knowledge, has never been demonstrated before. It also provided guidelines for the choice of the most relevant crystal plasticity model to use to accurately model a single crystal strain rate dependency, over a large strain-rate range, using a limited amount of material. The proposed methodology will therefore be applied on materials for which single crystals are more difficult to produce in future studies.

5. Conclusion

The objective of this work was to investigate the possibility to identify crystal plasticity strain-rate dependent parameters by FEMU using high strain rate micropillar compression experiments. The main contributions are as follows:

- Crystal plasticity strain rate sensitivity coefficients were identified for copper single crystals by FEMU using microcompression tests at strain rates up to 10^2 s^{-1}.
- The quality of the identification in terms of uniqueness and stability was assessed using an identifiability indicator.
- Identification using only compression in the [100] crystal orientation was sufficient to obtain a unique and stable solution for the strain-rate sensitivity coefficients.
- The satisfying quality of the solution was attributed to a strain rate sensitivity enhancing structural effects resulting from shear band strain localization.
- Experimental compressions revealed a strong influence of crystal orientation on the material's apparent strain-rate sensitivity.

Our experimental procedure only allowed to reach strain rates up to 10^2 s^{-1}. This is partly related to copper highly ductile behaviour, implying low load values in comparison to stiffer materials (such as silica glass [21]). To reach higher strain rates, identification using alternative experimental set-ups (such as micro-percussion or single shot canon) will be investigated.

Also, the model could not account for the material's yield stress strain rate dependency, nor for the high orientation influence on strain rate sensitivity observed experimentally. The identification procedure will be tested using alternative crystal plasticity framework accounting for the yield stress strain rate dependency (such as presented by Khan et al. [17]).

Finally, the relevance of the identified coefficient will be assessed on a different loading case than that used for identification. This will be performed using single impact shot and micropercussion experiments.

CRediT authorship contribution statement

S. Breumier: Conceptualization, Methodology, Investigation, Software, Formal analysis, Writing - original draft. **S. Sao-Joao:** Methodology, Investigation, Writing - review & editing. **A. Villani:** Conceptualization, Software, Writing - review & editing. **M. Lévesque:**Conceptualization, Writing - review & editing, Supervision, Funding acquisition. **G. Kermouche:** Conceptualization, Methodology, Investigation, Writing - review & editing, Supervision, Funding acquisition.

Acknowledgement

The authors would like to thank G.Guillonneau and D.Frey for their advices on dynamical effects during high dynamic microcompression tests and the use of the Alemnis high dynamics apparatus, D.Piot for useful discussions on size effects plasticity mechanisms, M. Mondon and G. Blanc for their help regarding the sample preparation. This work was supported by the Natural Sciences and Engineering Research Council (NSERC) discovery grants Canada Research Chairs programs (grant number, RGPIN-06412-2016), the LABEX MANUTECH-SISE (ANR-10-LABX-0075) of Université de Lyon, within the program “Investissements d'Avenir” (ANR-11-IDEX-0007) operated by the French National Research Agency (ANR) and by l'EQUIPEX MANUTECH-USD (ANR-10-EQPX-36-01). Finally, the authors would like to thank the Region Auvergne-Rhône-Alpes for their financial support within the SCUSI project.

Data availability

All the simulation input files, the optimisation script and raw and treated experimental microcompression stress-strain curves, pillar dimensions and deformed images can be found at https://zenodo.org/record/3801034#.XsPF3BaxU5k and can be reused.

Appendix A. Model geometry convergence study

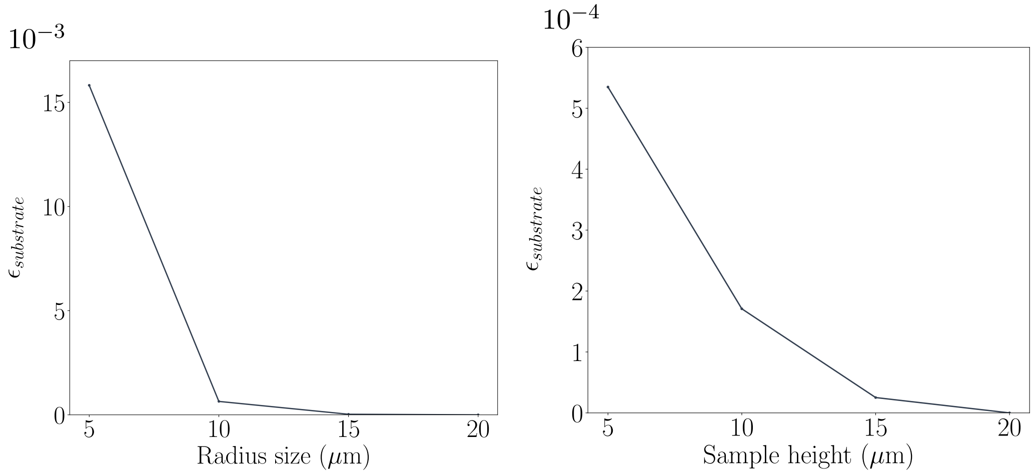

(a) *(b)*

Fig. 15. stress-strain curve error evolution with (a) the sample radius size and (b) the sample height. Negligible effect of the boundary conditions were found for h_{sub}=15 μm and R_{sub}=10 μm.

The substrate geometry dimensions h_{sub} and R_{sub} were chosen so that the influence of the boundary conditions on the stress-strain curve was negligible. Both dimensions of the substrate were therefore successively varied. The convergence criterion for the substrate geometry was chosen as:

$$\varepsilon_{substrate}\left(h_{sub,i},R_{sub,i}\right) = \frac{1}{T}\sum_{t=0}^{T}\left(\frac{\sigma_{conv}(\varepsilon(t)) - \sigma_{h_{sub,i}},R_{sub,i}(\varepsilon(t))}{max(\sigma_{conv})}\right)^2, \tag{14}$$

where σ_{conv} is the stress obtained using h_{sub}=20 μm and R_{sub}=20 μm and $\sigma_{h_{sub,\ i},\ R_{sub,\ i}}$ the stress obtained for $h_{sub,\ i}$ and $R_{sub,\ i}$ substrate dimensions.

Fig. 15 shows the evolution of ε with the variation of (a) the sample radius size and (b) the sample height. The substrate dimensions were chosen as h_{sub}=15 μm and R_{sub}=10 μm.

Appendix B. Mesh density convergence study

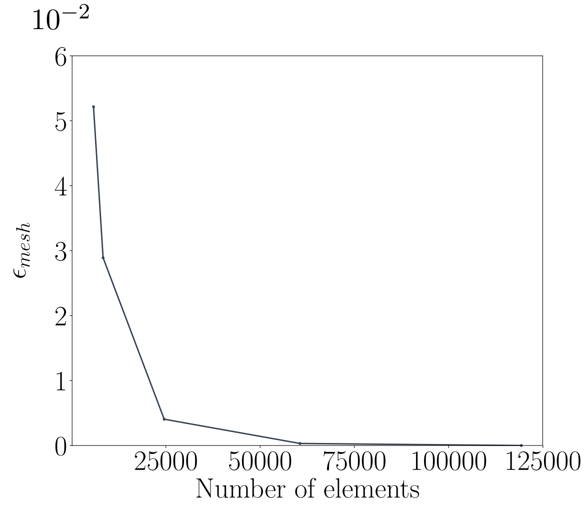

Fig. 16. Stress-strain curve sensitivity as a function of mesh size. Convergence can be observed for >25,000 elements.

The pillar mesh size was varied to assure that the computed stress-strain curve was independent of the number of elements. As previously, the convergence criteria was chosen as:

$$\varepsilon_{mesh}(N_{el}) = \frac{1}{T}\sum_{t=0}^{T}\left(\frac{\sigma_{conv}(\varepsilon(t)) - \sigma_{N_{el}}(\varepsilon(t))}{max(\sigma_{conv})}\right)^2, \tag{15}$$

where N_{el} is the number of elements and σ_{conv} is the stress obtained for 119,264 elements. Fig. 16 shows the evolution of the convergence criteria with the mesh size. Convergence was considered attained for 24,556 elements.

Appendix C. Influence of friction

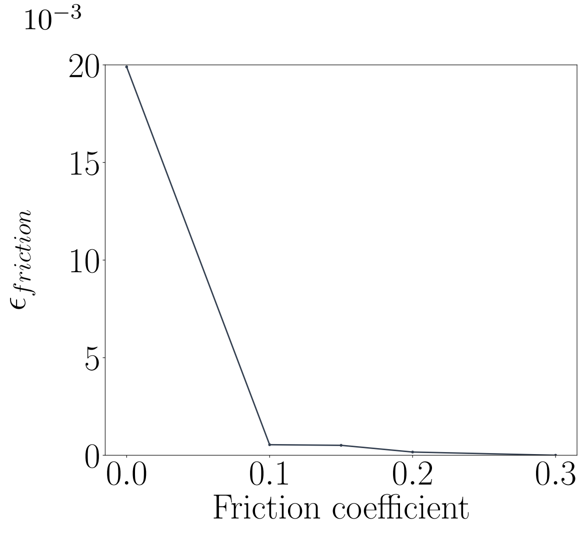

Fig. 17. Stress-strain curve sensitivity to the friction coefficient between the indenter and the pillar surface. Negligible influence of the coefficient value was found for values >0.1.

As the friction coefficient between the indenter and the pillar surface is very difficult to assess experimentally, a sensitivity analysis of the stress-strain curve to the friction coefficient was conducted. The stress-strain curve sensitivity to the friction coefficient was computed as:

$$\varepsilon_{friction}(\mu_s) = \frac{1}{T}\sum_{t=0}^{T}\left(\frac{\sigma_{conv}(\varepsilon(t)) - \sigma_{\mu_s}(\varepsilon(t))}{max(\sigma_{conv})}\right)^2, \tag{16}$$

where σ_{conv} is the stress obtained a friction coefficient μ_s=0.3.

Fig. 17 shows the variation of ε with the friction coefficient. As reported in the literature [28,40], the effect of the friction coefficient on the stress-strain curve is negligible. However, the absence of friction induces a very different behaviour as it generally leads to pillar buckling. In the present study the friction coefficient was therefore taken as μ_s=0.2, as pillar buckling is obtained numerically below this value and as no buckling was observed experimentally.

Appendix D. Size effects

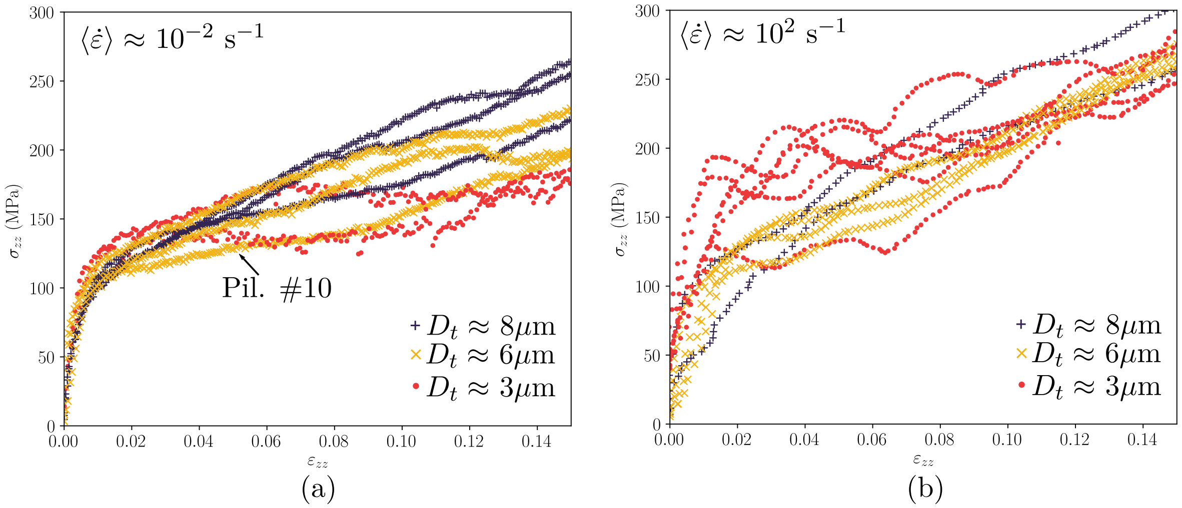

Fig. 18. Microcompression stress-strain curves for [110]-oriented pillars with 3,6 and 8 μm top diameters compressed at average strain-rates of (a) 10^{-2} s^{-1} and (b) 10^2 s^{-1}. At low strain rate, smaller pillars presented an almost perfectly plastic behaviour. At high strain rates, a 'smaller is stronger' effect was observed in most cases.

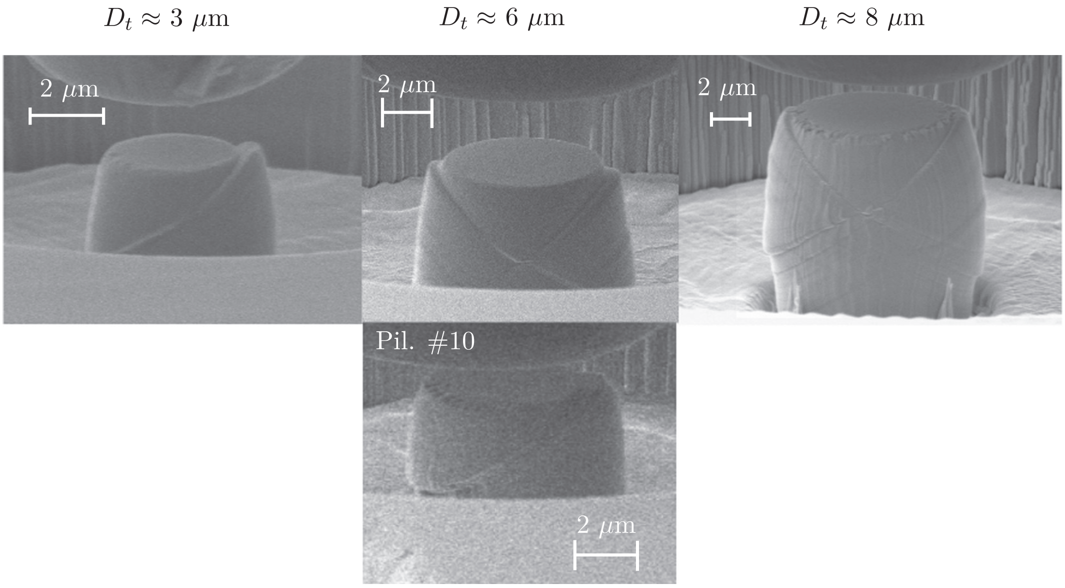

Fig. 19. 3 μm, 6 μm and 8 μm diameter pillars deformed shape after quasi-static compression in the [110] crystal orientation. Every 3 μm pillars presented a single slip band pattern. The 6 μm and 8 μm pillars exhibited double slip patterns only, except for the 6 μm diameter pillar #10.

Size effects were investigated to assure that the microcompression stress-strain curve obtained did not depend on the chosen pillar size. Pillars with three different diameters (3 μm 6 μm and 8 μm) were compressed in the [110] orientation at low (10^{-2} s^{-1}) and high (10^2 s^{-1}) strain rates to also investigate the compression rate influence on the potential size effects. The [110] orientation was chosen as fewer slip systems are activated when compressing in this orientation as compared with [100] and [111]. It is therefore more prone to starvation size effects. Fig. 18 shows the stress-strain curved obtained.

At low strain rates, 3 μm pillars presented a much lower hardening at the onset of plasticity than the bigger pillars. In overall, the 6 μm and 8 μm pillars presented similar hardening behaviours (except for 6 μm pillar #10 at low strain-rates).

To better understand the differences in hardening behaviour, the deformed shape of the pillars were considered. Fig. 19 presents the pillars deformed shapes associated to each curves at low strain rates. Most 3 μm pillars experienced the formation of a single slip band. Inversely, 6 μm and 8 μm pillars presented a double-slip behaviour. One of the three 6 μm pillar presented a single slip band. It corresponds to the only 6 μm pillar which presented only little hardening at the onset of plasticity at low strain rate (see Fig. 18).

Such differences in strain localization behaviour was already observed, experimentally and numerically, for smaller pillars by Kiener et al. [18]. According to the authors, for smaller pillar sizes, the initial dislocation densities for each gliding systems are not evenly distributed. This results in strain localization in systems where dislocation density is the highest. This induces a reverse size effect on the stress-strain curve.

Interestingly, at high strain rates, 3 μm pillars presented an overall stiffer behaviour as the bigger pillars. This could be related to a change in plasticity mechanism as the strain rate increases. Hu et al. [14] performed Discrete Dislocation Dynamics simulation of micropillar compression of submicronic copper pillars at different strain rates. According to the authors, at low strain rates, plasticity is driven by dislocation nucleation at sources. At higher strain rates, it is mainly driven by surface dislocation nucleation. However the strain rates amplitude used by the authors were higher and the pillar sizes were smaller than those used in this study. Also, validating such an assumption would require more tests to be conducted, owing to the statistical nature of dislocation distribution at this length scale. It is therefore beyond the scope of this study.

In the following, pillars presenting single slip in the studied orientation were not considered, as their strain mechanisms was not representative of the grain scale. Also, only 6 μm and 8 μm pillars were considered.

Appendix E. Single element simulation material parameter identification

To show the influence of the micropillar strain-rate enhancing structural effect developed in Section 4.1, the pillar was alternatively modeled as a single linear reduced hexaedric element (e.g. with a single integration point). Periodic boundary conditions were applied on the element faces. The experimental strain ε_{zz}, computed as:

$$\varepsilon_{zz} = \frac{u}{h_0}, \tag{17}$$

was imposed at the unique integration point. In Eq. (17), u and h_0 are respectively the experimental pillar displacement and the initial pillar height. This first approach was entirely modeled using the *Z*-set 8.6 software suite.

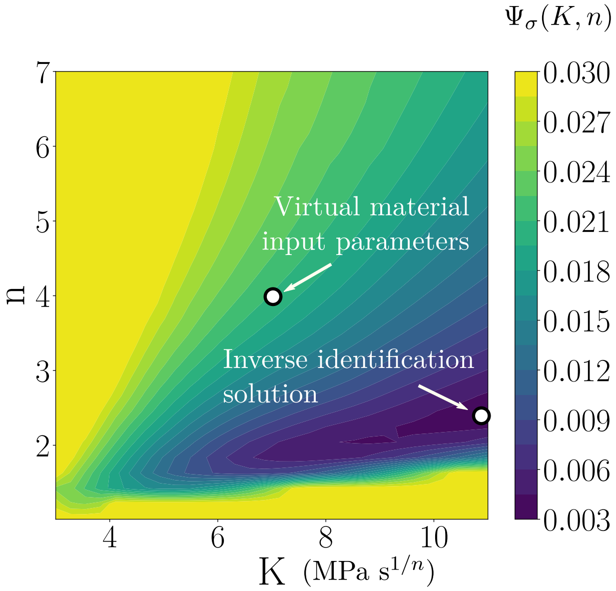

Fig. 20. Cost function Ψ_σ variation near the virtual material parameters, when performing identification of the K and n coefficients using the single element model. The identification solution was far from the virtual material parameters.

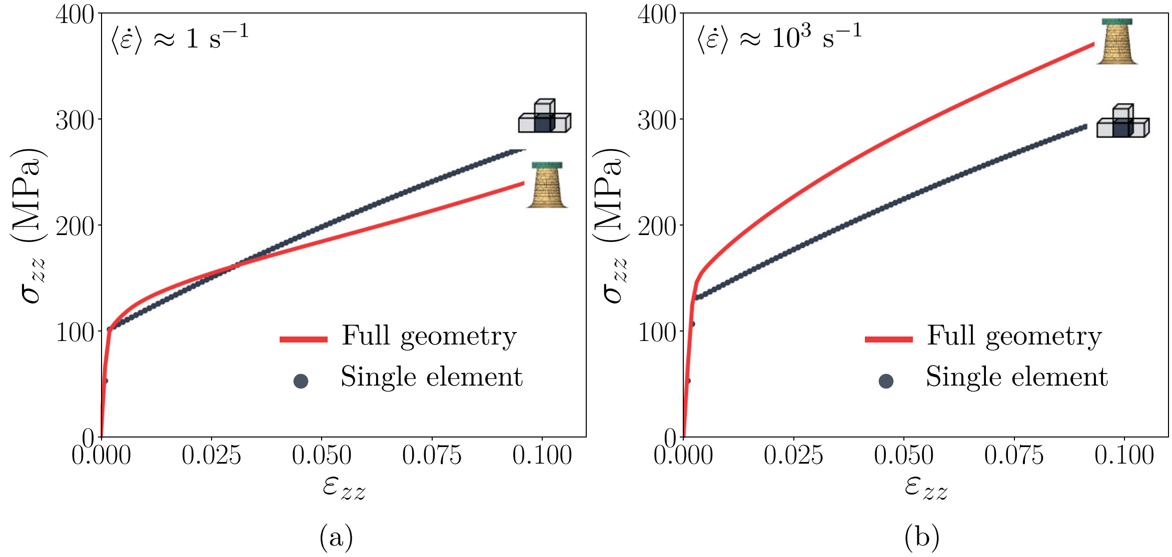

Fig. 21. Comparison of the numerical stress-strain curves obtained with the virtual material full-pillar geometry and the single-element simulations, using the [100] crystal orientation, at (a) $<\varepsilon> \approx 1\ \mathrm{s}^{-1}$ and (b) $<\varepsilon> \approx 10^3\ \mathrm{s}^{-1}$. The strain was computed using Eq. (17). The single element simulation presented a lower strain-rate sensitivity than when the whole pillar was modeled.

The inverse identification was performed on virtual data generated using the full pillar geometry model with $K = 7$ and $n = 4$. Fig. 20 shows the cost function Ψ_σ variations with coefficients K and n close to the virtual material solution. The figure reveals that the solution found by the identification procedure using a single element is very far from the chosen virtual material parameters. A factor two was found between the virtual material coefficients and the identified solution. Also, the cost function is stretched horizontally revealing a poor solution uniqueness.

To understand this bias induced by the identification procedure, single element simulations were performed with $K = 7$ and $n = 4$. Fig. 21 compares the numerical stress-strain curves obtained with the virtual material full-pillar geometry and the single-element simulations, using the [100] crystal orientation, at (a) $<\varepsilon> = 1\ \mathrm{s}^{-1}$ and (b) $<\varepsilon> = 10^3\ \mathrm{s}^{-1}$.

The single element simulation did not capture the strain-rate sensitivity observed using the full-pillar geometry. When using this model for identification, it therefore resulted in a very different solution than that expected. Such differences in the strain-rate sensitivity can be explained by a structural effect, as a single element simulation cannot account for the high strain rate concentration in the shear bands evidenced in Section 4.1.

Appendix F. High strain rate internal heat generation

The potential influence of internal heat generation in the pillar during high strain rate plastic straining on the measured mechanical properties was investigated. Heat generation during plastic straining in a material could be estimated using the coupled mechanical heat conduction equation given as [33]:

$$\rho C_p \frac{\partial T}{\partial t} = div(k\nabla T) + \beta(\sigma : \varepsilon^p), \tag{18}$$

where C_p is the specific heat taken as $386\ 10^6\ \mathrm{mm}^2\ \mathrm{s}^{-2}\ \mathrm{K}^{-1}$, ρ is the material's density chosen as $8.96\ 10^{-6} kg\ mm^{-3}$ for copper, T is the temperature, k is the thermal conductivity coefficient, β is a material constant and ε^p is the plastic strain rate.

Assuming that all plastic straining is converted into heat ($\beta = 1$) [16] and that, in the worst case, no conduction occurs the expected temperature derivatives would be of the order of $10^4 Ks^{-1}$ for $\varepsilon = 10^2\ s^{-1}$. The quickest tests performed in the present study lasting at most 4.8 ms, the expected temperature raise in the pillar should not exceed 48 K. Internal heat generation should therefore not have any influence on the tested material mechanical properties for the investigated strain rates.

References

[1] A. Barnoush, P. Hosemann, J. Molina-Aldareguia, J.M. Wheeler, In situ small-scale mechanical testing under extreme environments, MRS Bull. 44 (6) (2019) 471–477.

[2] S. Breumier, A. Villani, C. Maurice, M. Lévesque, G. Kermouche, Effect of crystal orientation on indentation-induced residual stress field: simulation and experimental validation, Mater. Des. 169 (2019) 107659.

[3] O. Casals, S. Forest, Finite element crystal plasticity analysis of spherical indentation in bulk single crystals and coatings, Comput. Mater. Sci. 45 (3) (2009) 774–782 (Proceedings of the 17th International Workshop on Computational Mechanics of Materials).

[4] A. Castro Moreno, F. Tu, M. Lévesque, P. Bocher, Shot peening fem simulation: a novel approach based on crystal plasticity, ICSP-13, 2017.

[5] A. Cruzado, B. Gan, M. Jiménez, D. Barba, K. Ostolaza, A. Linaza, J. Molina-Aldareguia, J. Llorca, J. Segurado, Multiscale modeling of the mechanical behavior of in 718 superalloy based on micropillar compression and computational homogenization, Acta Mater. 98 (2015) 242–253.

[6] J.A. El-Awady, M. Wen, N.M. Ghoniem, The role of the weakest-link mechanism in controlling the plasticity of micropillars, Journal of the Mechanics and Physics of Solids 57 (1) (2009) 32–50.

[7] A.M. Eleiche, M.M. Megahed, N.M. Abd-allah, The shot-peening effect on the HCF behavior of high-strength martensitic steels, J. Mater. Process. Technol. 113 (1–3) (2001) 502–508 (5th Asia-Pacific Conference on Materials Processing, Seoul, South Korea, 2001).

[8] E. Galindo-Nava, J. Sietsma, P.R.-D. del Castillo, Dislocation annihilation in plastic deformation: ii. Kocks–Mecking analysis, Acta Mater. 60 (6) (2012) 2615–2624.

[9] A. Giannakopoulos, P.-L. Larsson, R. Vestergaard, Analysis of Vickers indentation, Int. J. Solids Struct. 31 (19) (1994) 2679–2708.

[10] A. Guery, F. Hild, F. Latourte, S. Roux, Identification of crystal plasticity parameters using dic measurements and weighted femu, Mech. Mater. 100 (2016) 55–71.

[11] G. Guillonneau, M. Mieszala, J. Wehrs, J. Schwiedrzik, S. Grop, D. Frey, L. Philippe, J.-M. Breguet, J. Michler, J.M. Wheeler, Nanomechanical testing at high strain rates: new instrumentation for nanoindentation and microcompression, Mater. Des. 148 (2018) 39–48.

[12] S.M. Hassani-gangaraj, K.S. Cho, H.J.L. Voigt, M. Guagliano, C.A. Schuh, Experimental assessment and simulation of surface nanocrystallization by severe shot peening, Acta Mater. 97 (2015) 105–115.

[13] M. Horstemeyer, M. Baskes, A. Godfrey, D. Hughes, A large deformation atomistic study examining crystal orientation effects on the stress–strain relationship, Int. J. Plast. 18 (2) (2002) 203–229.

[14] J. Hu, Z. Liu, E.V. der Giessen, Z. Zhuang, Strain rate effects on the plastic flow in submicron copper pillars: considering the influence of sample size and dislocation nucleation, Extreme Mechanics Letters 17 (2017) 33–37.

[15] S. Hu, C. Guo, D. Wang, Z. Wang, C. Huang, Finite element analysis of residual stress evolution with multiple impacts on one point in ultrasonic impact treatment process, Proc. Inst. Mech. Eng. B J. Eng. Manuf. 232 (7) (2018) 1201–1211.

[16] R. Kapoor, S. Nemat-Nasser, Determination of temperature rise during high strain rate deformation, Mech. Mater. 27 (1) (1998) 1–12.

[17] A.S. Khan, J. Liu, J.W. Yoon, R. Nambori, Strain rate effect of high purity aluminum single crystals: experiments and simulations, Int. J. Plast. 67 (Supplement C) (2015) 39–52.

[18] D. Kiener, P. Guruprasad, S. Keralavarma, G. Dehm, A. Benzerga, Work hardening in micropillar compression: in situ experiments and modeling, Acta Mater. 59 (10) (2011) 3825–3840.

[19] U. Kocks, H. Mecking, Physics and phenomenology of strain hardening: the fcc case, Prog. Mater. Sci. 48 (3) (2003) 171–273.

[20] B. Kondori, A. Needleman, A.A. Benzerga, Discrete dislocation simulations of compression of tapered micropillars, Journal of the Mechanics and Physics of Solids 101 (2017) 223–234.

[21] R. Lacroix, V. Chomienne, G. Kermouche, J. Teisseire, E. Barthel, S. Queste, Micropillar testing of amorphous silica, Int. J. Appl. Glas. Sci. 3 (1) (2012) 36–43.

[22] J. Lu, S. Suresh, G. Ravichandran, Dynamic indentation for determining the strain rate sensitivity of metals, Journal of the Mechanics and Physics of Solids 51 (11) (2003) 1923–1938 (Proceedings of a Symposium on Dynamic Failure and Thin Film Mechanics, honoring Professor L.B. Freund).

[23] S. Meguid, G. Sagals, J. Stranart, 3D finite element analysis of peening of strain-rate sensitive materials using multiple impingement model, International Journal of Impact Engineering 27 (119–134) (2002) 02.

[24] M.A. Meyers, Dynamic Behavior of Materials, John Wiley & Sons, Inc, 1994.

[25] L. Méric, G. Cailletaud, M. Gaspérini, Finite element calculations of copper bicrystal specimens submitted to tension-compression tests, Acta Metall. Mater. 42 (3) (1994) 921–935.

[26] W.D. Musinski, D.L. McDowell, On the eigenstrain application of shot-peened residual stresses within a crystal plasticity framework: application to ni-base superalloy specimens, Int. J. Mech. Sci. 100 (Supplement C) (2015) 195–208.

[27] M.-J. Pac, S. Giljean, C. Rousselot, F. Richard, P. Delobelle, Microstructural and elasto-plastic material parameters identification by inverse finite elements method of ti(1-x) alxn (0<x<1) sputtered thin films from berkovich nano-indentation experiments, Thin Solid Films 569 (2014) 81–92.

[28] D. Raabe, D. Ma, F. Roters, Effects of initial orientation, sample geometry and friction on anisotropy and crystallographic orientation changes in single crystal microcompression deformation: a crystal plasticity finite element study, Acta Mater. 55 (13) (2007) 4567–4583.

[29] S. Rawat, S. Chandra, V.M. Chavan, S. Sharma, M. Warrier, S. Chaturvedi, R.J. Patel, Integrated experimental and computational studies of deformation of single crystal copper at high strain rates, J. Appl. Phys. 116 (21) (2014), 213507.

[30] E. Renner, A. Bourceret, Y. Gaillard, F. Amiot, P. Delobelle, F. Richard, Identifiability of single crystal plasticity parameters from residual topographies in berkovich nanoindentation on fcc nickel, Journal of the Mechanics and Physics of Solids 138 (2020), 103916.

[31] E. Renner, Y. Gaillard, F. Richard, F. Amiot, P. Delobelle, Sensitivity of the residual topography to single crystal plasticity parameters in berkovich nanoindentation on fcc nickel, Int. J. Plast. 77 (Supplement C) (2016) 118–140.

[32] F. Richard, M. Villars, S. Thibaud, Viscoelastic modeling and quantitative experimental characterization of normal and osteoarthritic human articular cartilage using indentation, J. Mech. Behav. Biomed. Mater. 24 (2013) 41–52.

[33] E. Rouhaud, A. Ouakka, C. Ould, J. Chaboche, M. François, Finite elements model of shot peening, effects of constitutive laws of the material, Proceedings ICSP-9, Paris, France, 1, , 2005.

[34] T. Rousseau, C. Nouguier-Lehon, P. Gilles, T. Hoc, Finite element multi-impact simulations using a crystal plasticity law based on dislocation dynamics, Int. J. Plast. 101 (2017) 42–57 pages–.

[35] P. Sanjurjo, C. Rodriguez, I. Penuelas, T. Eduardo Garcia, F. Javier Belzunce, Influence of the target material constitutive model on the numerical simulation of a shot peening process, Surface & Coatings Technology 258 (2014) 822–831.

[36] Q. Shi, F. Latourte, F. Hild, S. Roux, Backtracking depth-resolved microstructures for crystal plasticity identification—part 2: identification, JOM 69 (12) (2017) 2803–2809 Dec.

[37] Y. Tirupataiah, G. Sundararajan, A dynamic indentation technique for the characterization of the high strain rate plastic flow behaviour of ductile metals and alloys, Journal of the Mechanics and Physics of Solids 39 (2) (1991) 243–271.

[38] D. Tumbajoy-Spinel, X. Maeder, G. Guillonneau, S. Sao-Joao, S. Descartes, J.-M. Bergheau, C. Langlade, J. Michler, G. Kermouche, Microstructural and micromechanical investigations of surface strengthening mechanisms induced by repeated impacts on pure iron, Mater. Des. 147 (2018) 56–64.

[39] Z. Wang, I. Beyerlein, R. LeSar, Plastic anisotropy in fcc single crystals in high rate deformation, Int. J. Plast. 25 (1) (2009) 26–48.

[40] H. Zhang, B. Schuster, Q. Wei, K. Ramesh, The design of accurate micro-compression experiments, Scr. Mater. 54 (2) (2006) 181–186.

[41] J. Zhang, S. Lu, T. Wu, Z. Zhou, W. Zhang, An evaluation on sp surface property by means of combined fem-dem shot dynamics simulation, Adv. Eng. Softw. 115 (Supplement C) (2018) 283–296.

[42] Z. Zhang, T.-S. Jun, T.B. Britton, F.P. Dunne, Intrinsic anisotropy of strain rate sensitivity in single crystal alpha titanium, Acta Mater. 118 (2016) 317–330.